

Dynamic magnetic fields transform pivoting H_2SiO_3 particles to hollow microspheres with nanofibrous interior

Received: 21 February 2025

Xiaohua Qiao, Rui Feng Qi, Junqi Liu & Qingsong Huang  

Accepted: 25 November 2025

Published online: 11 December 2025

 Check for updates

Reorganizing the internal structures of hollow microspheres after shell sealing, without damaging the shell, remains a major challenge. Here, we show a dynamic magnetic field fluxes stirring (DMFFS) technology that can transform H_2SiO_3 particle to a sealed SiO_2 hollow microsphere with fibrous interior within 30 s. The fibrous structure is composed of SiO_2 micro-nano fibers (MNF). As dynamic magnetic field drives the SiO_2 particles to rotate, the rotated SiO_2 particles become magnetized along the rotation axis according to the Barnett effect. Magnetized SiO_2 interacts with magnetic field to form fibers. This MNF-structured microsphere exhibits low density (0.1 g cm^{-3}), high transparency (ca. 85.6%), superior thermal stability ($1200\text{ }^\circ\text{C}$) and thermal insulation performance. Fluorescent additives can be uniformly incorporated into the MNF-structured microspheres, enabling distinctive and reproducible fluorescent functionality. In addition, a sealed SiO_2 hollow microsphere with nanofibrous interior can be obtained by extending the stirring time or increasing the magnetic field strength. The DMFFS process provides an alternative route to rapidly produce mass SiO_2 microspheres containing SiO_2 micro/nano-sized fibers. Furthermore, our findings have provided an insight for manipulating non-magnetic materials.

Intricate hollow structures have garnered significant interest owing to their diverse characteristics, distinctive physicochemical properties and potential applications in catalysis^{1–3}, energy storage^{4–7}, drug delivery^{8–10} and related field^{11–14}. Based on their internal structure characteristics, they can be classified into hierarchical hollow structure^{14–16}, multi-cores structure^{17–20}, multi-chamber structure^{21–23}, multi-shell structure^{24,25} and others. In pursuit of practical applications, the hollow structures are continuously engineered for complexity. For example, Chen et al. developed an electrospray technique to enclose different components into a single microcapsule²¹. Wei et al. designed $\text{SrTiO}_3@\text{TiO}_2$ heterogeneous hollow multi-shell structures, which exhibited superior overall water splitting performance²⁴. The SiO_2 fibers can be adopted to thermal insulation material due to their high temperature tolerance, high transparency, and antioxidant capacity, etc.²⁶. Incorporating SiO_2 fibers into hollow spheres improves their 3D spatial arrangement and ensures isotropic uniformity. Therefore, SiO_2

fiber-filled spheres are more conducive to forming dense pile structures, directly improving thermal insulation efficiency.

Although many technologies, such as template-assisted^{27–29}, self-assembly^{1,30,31}, three-dimensional (3D) printing^{20,32}, have been developed for constructing intricate hollow structures, these methods require constructing the internal structure first and then sealing it with shell. However, it remains a big challenge to transform solid particles directly into encapsulated fibers within hollow spheres, let alone non-magnetic particles. In this paper, a smart DMFFS technique has been developed to manipulate the dynamic magnetic fluxes, which can be adopted to interfere with the semi-molten SiO_2 into a sealed hollow microsphere with fiber structure inside. The internal fiber structure can be further refined by extending the stirring time or increasing the magnetic field strength.

Dynamic magnetic field refers to a kind of magnetic field that varies with time periodically. It can be applied to heat materials,

indicating the raw materials can be transformed to semi-molten or molten state during the DMFFS process. Meanwhile, dynamic magnetic field can interact with the semi-molten or molten materials, even if the materials are composed of non-magnetic substances such as SiO_2 . According to the Maxwell-Ampère's law, the variable dynamic magnetic field (\mathbf{B}_1) generates electric vector (\mathbf{E}). When SiO_2 is molten, the \mathbf{E} vector drives polarized SiO_2 molecules aligned along with the vector orientation. Once the direction of \mathbf{E} vector changes, the displacement current (\mathbf{I}_D) will be generated, which can lead SiO_2 to spin subsequently. The molten SiO_2 initiates the random clockwise or counterclockwise spinning. The spinning SiO_2 will become magnetized according to the Barnett effect, and the spinning particles will interact with dynamic magnetic field. The semi-molten SiO_2 owns opportunity to be transformed into 1D fibers under the dynamic magnetic field (Supplementary Fig. 1). In this context, Liang et al.³³ extracted crystalline Si nanowires with a diameter of 30–50 nm from Ti_3SiC_2 . Zhou et al.³⁴ isolated high quality 1D amorphous Si nanowires from SiC in 1 min. Qiao et al.³⁵ extracted SiC /amorphous SiO_2 core-shell nanowires from rice husk ash within 25 s. These results indicate that a dynamic magnetic field can interact with non-magnetic materials to form nanowires.

Herein, the H_2SiO_3 particles were heated and dehydrated gradually to SiO_2 , and then became molten state and spun. Subsequently, they were stirred by dynamic magnetic fluxes to form a sealed hollow SiO_2 microsphere full of MNF structure. By DMFFS process, the outer layer of H_2SiO_3 particles were heated to SiO_2 at 15 s (SiO_2 -15). Then the decomposed and molten SiO_2 layer gradually transformed to a sealed shell. Successively, the SiO_2 -15 particles evolved into microspheres with a multi-chamber structure at 20 s (MC20 microsphere). As the DMFFS process continues for 10 s (a total time of 30 s), the shell expanded continuously and the MC20 structure was reconstructed into MNF structure (MNF-structured microsphere). The tapped density of MNF-structured microsphere was just 0.1 g cm^{-3} , which was much lower than that of quartz (2.2 g cm^{-3}). The MNF-structured microspheres exhibited a high transparency of $\approx 85.6\%$. The MNF-structured microspheres could be preserved perfectly under $1200\text{ }^\circ\text{C}$ in the air and argon atmosphere. The structure and thermal stability offered a thermal insulation performance. In addition, the SrAl_2O_4 ingredients could be homogeneously incorporated into MNF structure and its shell, for distinctive fluorescence performance and used for anti-counterfeiting material. It was critical that when an MC20 microsphere

underwent the DMFFS process for 30 s, the MNF structure was further transformed into a SiO_2 NF structure within a sealed microsphere. Furthermore, spinning built the interaction between dynamic magnetic field and non-magnetic materials, as those spinning particles could be magnetized according to the Barnett effect.

Results

Syntheses and structural characterization

When the exciting magnetic current in induction furnace was set around 20 A (AC), the generated dynamic magnetic field would heat the graphite crucible (Fig. 1a and Supplementary Movie 1). Thus, the H_2SiO_3 particles (Supplementary Fig. 2) were heated from the outer layer to center and dehydrated to form a new particle at 15 s (SiO_2 -15, Supplementary Fig. 3). The X-ray diffraction (XRD pattern, Supplementary Fig. 4a) and Raman spectra (Supplementary Fig. 4b) proved the SiO_2 -15 included both amorphous SiO_2 and H_2SiO_3 . The outer layer of SiO_2 -15 particle was molten and formed a shell quickly by continuous heating. Under DMFFS for 20 s, the internal H_2SiO_3 in particles became decomposed and the water vapor was blocked due to the semi-molten SiO_2 shell with increased temperature. The semi-molten SiO_2 shell expanded and its thickness was about $30\text{ }\mu\text{m}$ (Fig. 2a and Supplementary Fig. 5). Immediately after that, the MC20 structure would be formed (Fig. 2b, c). The microsphere obtained at 20 s was denoted as MC20 microsphere.

After 20 s, the MC20 microspheres exhibited a “jumping” phenomenon, suggesting magnetizing process began to work according to the Barnett effect. Then, the MC20 microspheres began to suspend and rotate as shown in Supplementary Movie 1. The rotating microsphere was further driven to swell and transform into a transparent microsphere at 30 s, and the thickness of shell was about $5\text{ }\mu\text{m}$ (Supplementary Fig. 6, Fig. 2d, e inset). Meanwhile, the MC20 structure was transformed into the MNF structure by the DMFFS process without damaging its shell (Fig. 2e, f). The MNF structure was composed of plentiful micro-nano fibers with diameter ranging from 30 nm to $25\text{ }\mu\text{m}$ (Fig. 2f and Supplementary Fig. 7). The obtained microsphere at 30 s was denoted as MNF-structured microsphere, which was composed of amorphous SiO_2 (Supplementary Figs. 4, 8, 9). The fabrication process of MNF-structured microsphere could be repeated many times (Supplementary Fig. 10 and Supplementary Movies 2–4).

To further refine the MNF structure to NF, the MC20 microspheres were returned to induction furnace for DMFFS processing at

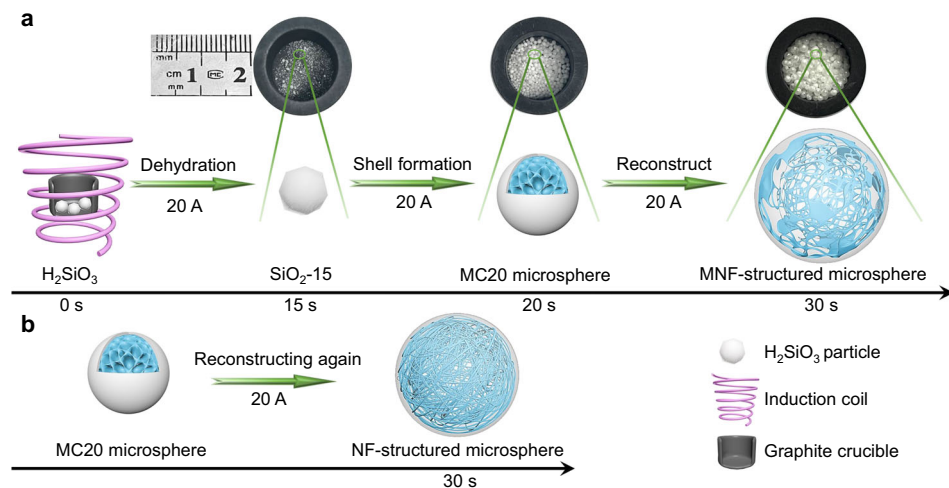


Fig. 1 | The diagram of reconstructing processes. **a** MNF: the H_2SiO_3 particles gradually became an MNF-structured microsphere after dehydration, shell formation, and reconstruction. The size of the MNF-structured microsphere reached its maximum at 30 s and the shell turned to be transparent. The time from MC20

microsphere to MNF-structured microsphere was only 10 s. **b** NF: the MC20 structure was reconstructed further within 30 s at 20 A (AC) by refining the internal fibers into nanofibers. The time from MC20 microsphere to NF-structured microsphere was 30 s.

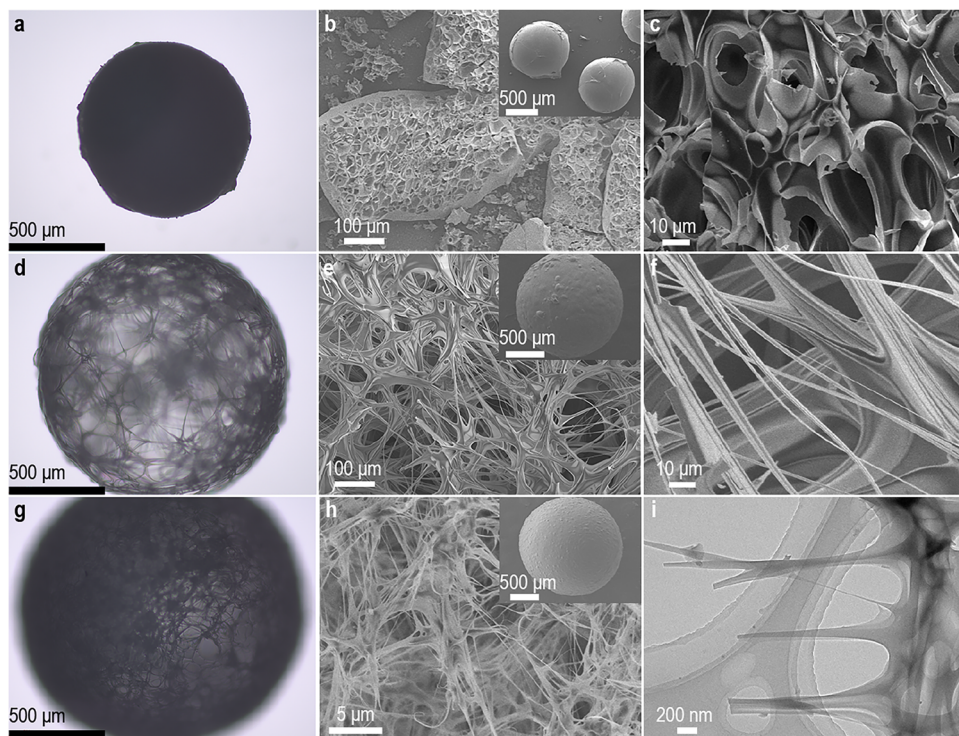


Fig. 2 | Morphology character of MNF-structured microsphere and NF-structured microsphere. **a** The optical microscope image of a non-transparent MC20 microsphere. **b, c** The structure inside the MC20 microsphere. **d** The optical microscope image of a transparent MNF-structured microsphere. **e, f** The MNF

structure inside the microsphere. **g** The optical microscope image of a transparent NF-structured microsphere. **h** The NF structure inside the microsphere. **i** TEM image of the NF structure inside NF-structured microsphere. All experiments were independently repeated a minimum of three times.

room temperature, with the treatment conducted for 30 s at 20 A (AC) (Fig. 1b). This transparent microsphere was denoted as NF-structured microsphere, while its shell remained intact (Fig. 2g and Fig. 2h inset). The NF structure with diameter ranging from 50 nm to 600 nm (Fig. 2h, i, Supplementary Fig. 11). As shown in Supplementary Figs. 12, 13, the HRTEM and EDS results confirmed the structure was composed of amorphous SiO₂. Furthermore, similar NF-structured microsphere also could be obtained by increasing the magnetic field strength (Supplementary Fig. 14).

As a control, the H₂SiO₃ particles were heated to 1100 °C, imitating the induction temperature, and maintained for 1 min in a tube furnace to produce SiO₂-1100 °C particle (Supplementary Fig. 15). Both the outer size and the volume of the SiO₂-1100 °C particle were maintained and no interior fibers were observed (Supplementary Fig. 16). The sample was further characterized by XRD (Supplementary Fig. 17) and XPS (Supplementary Fig. 18), confirming that it consisted of amorphous SiO₂. This result proved that MNF-structured microsphere was formed through the synergistic effect of heating and DMFFS, rather than by heating only.

To directly observe the interaction between the dynamic magnetic field and non-magnetic microsphere, the sample MC20 microspheres were returned to furnace and undergone DMFFS process at 27 A (AC) for 40 s. It should be pointed out the MC20 samples were composed of amorphous SiO₂, as well as a small amount of water. The evolution of the MC20 microspheres under DMFFS at 27 A was shown in Fig. 3a and Supplementary Movie 5. For the topmost lined circles in Fig. 3a, the circle profile represents the heating crucible, and the white particles are MC20 microsphere samples.

During the stage 1 (0–10 s), the surfaces of MC20 microspheres were heated to a semi-molten state. According to Maxwell-Ampère's law, the molten SiO₂ molecules began to pivot around their axis. The MC20 microspheres were magnetized by spinning according to the Barnett effect.

In the stage 2 (10–13 s), the shell of the MC20 microspheres expanded while remaining sealed. The magnetized MC20 microspheres suspended in the graphite crucible (Supplementary Movie 5, Fig. 3a). Then, the high-speed rotation of magnetized MC20 microspheres enabled the internal molten SiO₂ to be stirred by dynamic magnetic fluxes, resulting in formation of a MNF structure.

In stage 3 (after 13 s), the MNF-structured microspheres fully melted into liquid status, and lost their structure integrity (Fig. 3b, c). Finally, the collapsed SiO₂ microspheres spun increasingly faster under electromagnetic force. It was interesting that while the spinning orientation was random, once the pivoting was triggered, all collapsed SiO₂ microspheres rotated in a fixed direction. The collapsed SiO₂ microspheres remained amorphous (Fig. 3d and Supplementary Fig. 19).

The magnetic property characterization was performed via the physical property measurement system (PPMS). The hysteresis loop (M-H) curves for the SiO₂-1100 °C, MC20 microspheres, and collapsed SiO₂ microspheres were collected at 300 K from -3 T to 3 T, respectively. The typical diamagnetic background was found (Fig. 3e). In addition, the MC20 microspheres and the collapsed SiO₂ microspheres had demonstrated typical ferromagnetism momentum under diamagnetic background (Fig. 3e and Supplementary Fig. 20). The saturation magnetization intensity could not be observed directly at high excitation magnetic fields. Thus, the hysteresis loop curves by deducting the linear background were demonstrated in Fig. 3f. For SiO₂-1100 °C, the saturation magnetization intensity and the hysteresis loop were almost approaching zero, suggesting it was impossible to magnetize SiO₂ by heating alone.

However, for MC20 microspheres, the saturation magnetization intensity increased substantially to 6.28×10^{-3} emu g⁻¹. In addition, the hysteresis loop of collapsed SiO₂ microspheres was significantly enhanced, referring to the hysteresis loop curve at 5 K. Measurements of the increased momentum revealed a saturation magnetization of

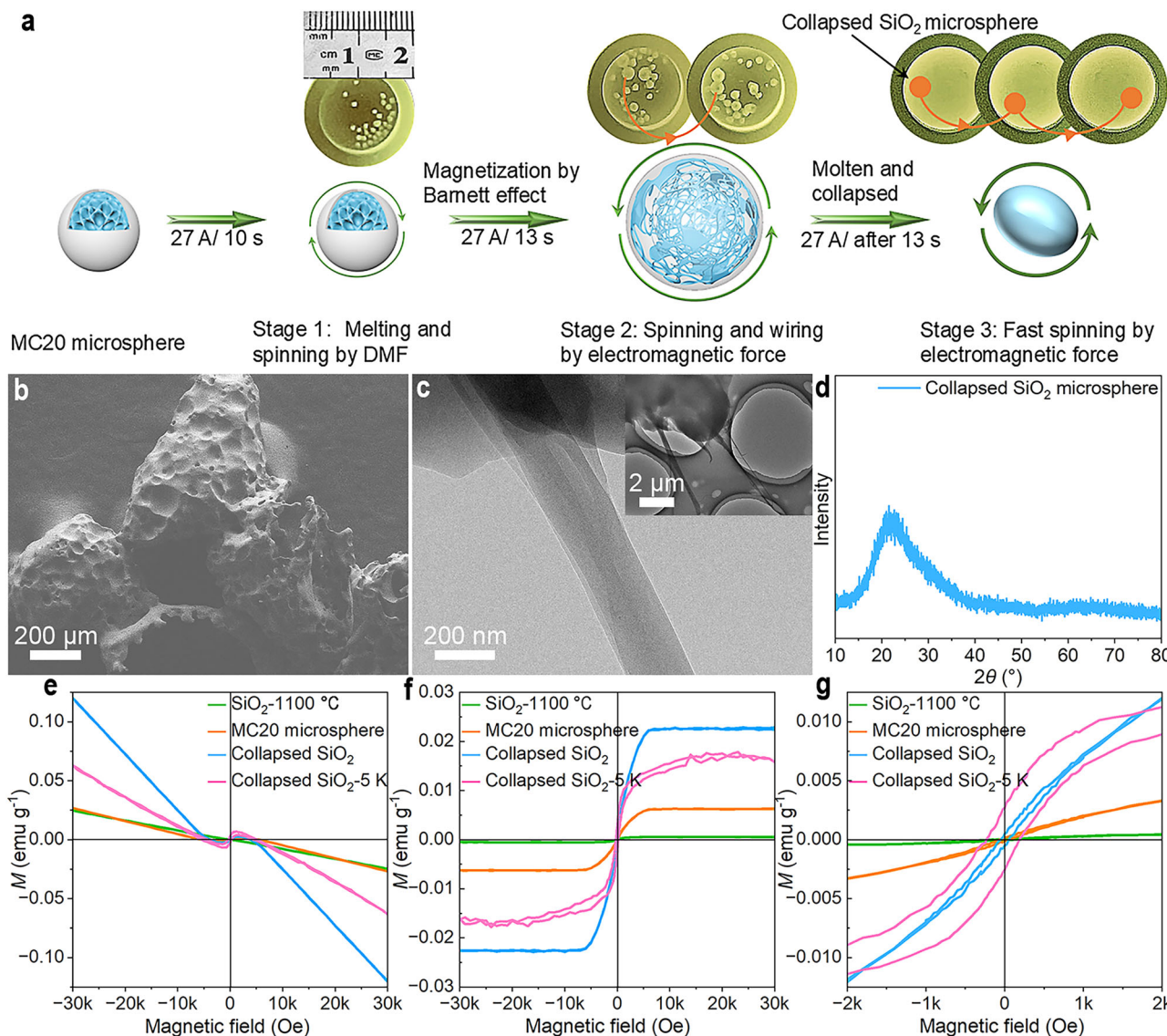


Fig. 3 | Magnetization mechanism of non-magnetic SiO_2 microsphere. **a** The diagram of the magnetization process of non-magnetic SiO_2 microsphere. Solid red circles exhibit the collapsed SiO_2 microsphere to make it clearly visible. **b** The SEM image of collapsed SiO_2 microsphere. The experiment was independently repeated a minimum of three times. **c** The TEM image of collapsed SiO_2 microsphere. The experiment was independently repeated a minimum of three times. **d** The XRD pattern of collapsed SiO_2 microsphere. **e** The hysteresis loop curves (the original

curves) of SiO_2 -1100 °C (green) at 300 K, MC20 microsphere (orange) at 300 K, collapsed SiO_2 microsphere (blue) at 300 K and collapsed SiO_2 microsphere (pink) at 5 K. **f** The hysteresis loop curves (the signal of the diamagnetic backing is deducted) of SiO_2 -1100 °C (green) at 300 K, MC20 microsphere (orange) at 300 K, collapsed SiO_2 microsphere (blue) at 300 K and collapsed SiO_2 microsphere (pink) at 5 K. **g** Was a local enlargement in (f). Source data are provided as a Source Data file.

$1.6 \times 10^{-2} \text{ emu g}^{-1}$ (Fig. 3f), a coercive force of 200.2 Oe (Fig. 3g), and a remanent magnetization of $2.65 \times 10^{-3} \text{ emu g}^{-1}$ (Fig. 3g). These results proved that molten SiO_2 could be stimulated to magnetization and interacted with dynamic magnetic field intrinsically.

The combined thermogravimetric analysis (TGA), differential scanning calorimetry (DSC) and mass spectrometry (MS) of the MNF-structured microspheres were tested under air atmosphere. The TGA curve showed the total mass loss of the MNF-structured microspheres was only 1.32% at 1450 °C (Fig. 4a). The mass loss before 276 °C was mainly due to the evaporation of surface adsorbed water^{36,37}. The MNF-structured microspheres became soft and deformable when heated to 1229 °C, and released water vapor from the internal pore structure. At this temperature, the microspheres were semi-molten with higher viscosity than in the molten state. Due to the high viscosity of semi-molten SiO_2 , the inner water vapor gradually penetrated through the obstacle between the pores and shell. Upon the further heating, the

MNF-structured microspheres completely melted, and the shell could no longer support its weight, leading to structural collapse and release of water vapor (Supplementary Fig. 21). The DSC curve also exhibited two exothermal peaks at 276 °C and 1229 °C, corresponding to two stages of water loss. Mass spectrometry further confirmed these results by monitoring the molecular of H_2O . H_2O emission occurred at 1229 °C (Fig. 4b), indicating that a small amount of water vapor was sealed within the shell during the formation of the MNF-structured microsphere.

The FT-IR spectrum of MNF-structured microspheres displayed an intense peak at 1047.3 cm^{-1} , corresponding to the asymmetric stretching vibration of the Si-O bond in SiO_2 . The band at 801.9 cm^{-1} was assigned to the characteristic Si-O-Si stretching vibration, while the peaks locating in the range of 300 cm^{-1} to 600 cm^{-1} were attributed to the swing vibrations of the Si-O bond of SiO_2 (Fig. 4c). The survey XPS of the MNF-structured microspheres revealed the peaks arising

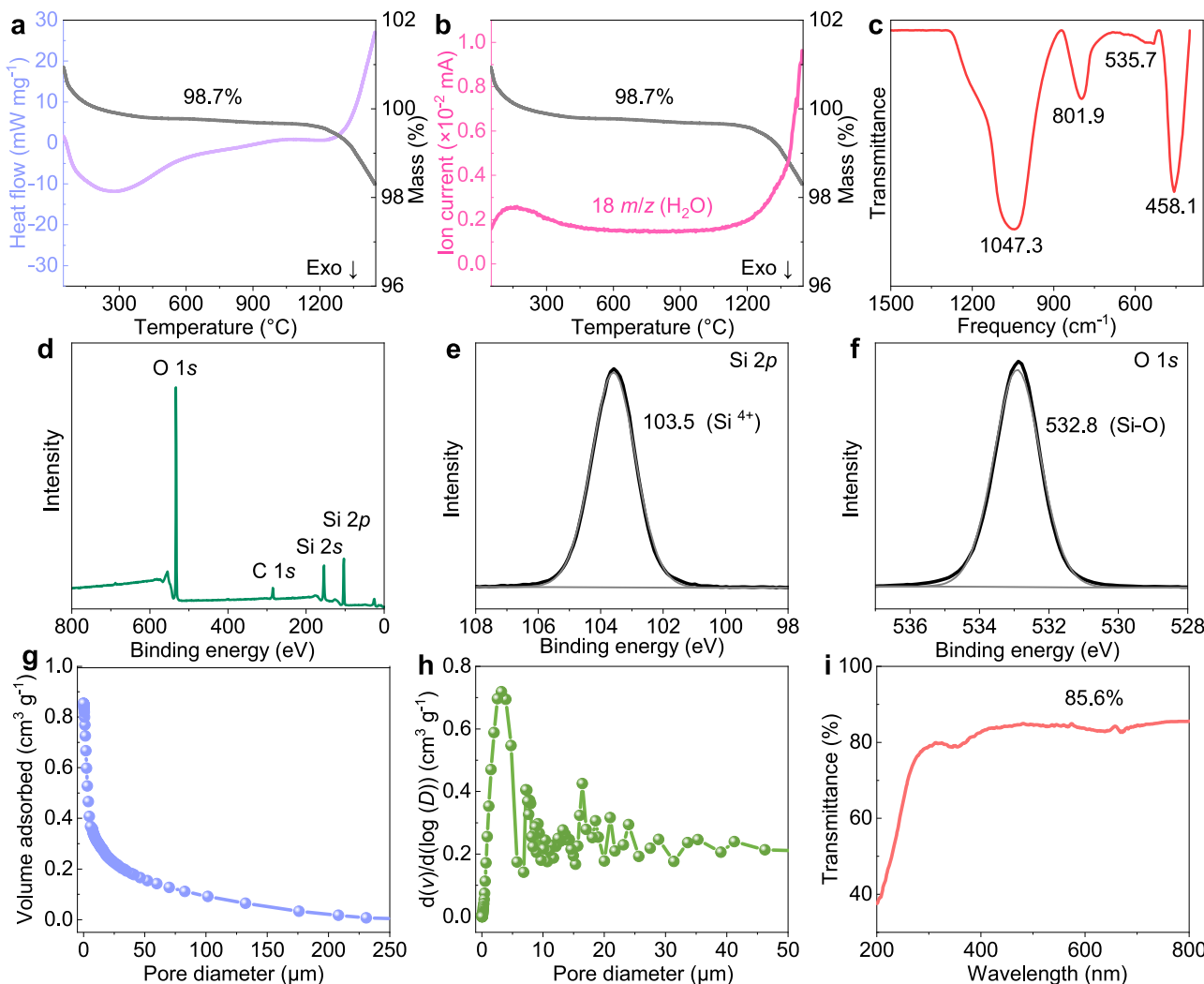


Fig. 4 | Characteristics and related performance of the MNF-structured microsphere. **a** The TGA and DSC curve of the MNF-structured microsphere (the gray represented TGA curve, the purple represented DSC curve). The initial TGA weight exceeded 100% due to a 50-min purge with high-purity air, which affected the sample's initial mass. This effect was negligible. **b** The TGA and MS curve of the MNF-structured microsphere (the gray represented TGA curve, the pink represented MS curve). The Exo of (a, b) stands for the exothermic reaction. **c** FT-IR

spectrum of MNF-structured microsphere. **d** Survey XPS, **e** high-resolution Si 2p, **f** high-resolution O 1s of MNF-structured microsphere. **g** the cumulative pore size distribution (CPSD) curve of the MNF-structured microsphere, **h** The differential pore size distribution (DPSD) curve of the MNF-structured microsphere. **i** The total transmittance in visible range of the MNF-structured microsphere. Source data are provided as a Source Data file.

from Si, O, and trace quantities of C (Fig. 4d). The high-resolution Si 2p spectrum showed a peak at 103.6 eV, which conformed to the characteristic of Si^{4+} (Fig. 4e)^{38,39}. Combined with the high-resolution O 1s spectrum (Fig. 4f), those results confirmed that the MNF-structured microspheres were composed of amorphous SiO_2 . Both XPS and FT-IR spectra results showed that no new component formed during microspheres preparation.

The tap density of the MNF-structured microspheres was 0.1 g cm^{-3} calculated by measuring the average mass to the tap volume ratio in triplicate. The tap volume was obtained by raising the measuring cylinder 25 mm and allowing it to fall back to the horizontal plane, repeated ten times. The average porosity was calculated to be 95.5% using the following Eq. (1)⁴⁰:

$$\text{porosity} = (1 - \rho_a / \rho_s) \quad (1)$$

where ρ_a was the tap density, and ρ_s was the skeleton density (assumed to be 2.2 g cm^{-3} for SiO_2). Mercury intrusion porosimetry (MIP)⁴¹ results revealed that the pore size distribution range was mainly 0.5 to $50 \mu\text{m}$,

and the average pore size was $\approx 2.6 \mu\text{m}$ (Fig. 4g, h). The transparency of the MNF-structured microspheres could reach $\approx 85.6\%$ in the visible range (Fig. 4i).

Thermal properties

TGA was performed to evaluate the thermal stability of the MNF-structured microspheres. When heated to 1200°C at a rate of $10^\circ\text{C min}^{-1}$ in air atmosphere, the mass only increased slightly by 1.1%, which was due to instrumental error (Supplementary Fig. 22a). The shells and internal MNF structure remained intact, suggesting the thermal stability in air atmosphere (Supplementary Fig. 22b, c). In argon, the microspheres exhibited no detectable weight change upon heating from room temperature to 1200°C (Supplementary Fig. 22d), and the morphology was persevered (Supplementary Fig. 22e, f). These results indicated that the MNF-structured microspheres exhibited superior thermal stability up to 1200°C in both air and argon atmosphere.

The MNF-structured microspheres presented a hollow structure and thermal stability, which offered a thermal insulation performance. As a proof-of-concept for thermal insulation, MNF-structured

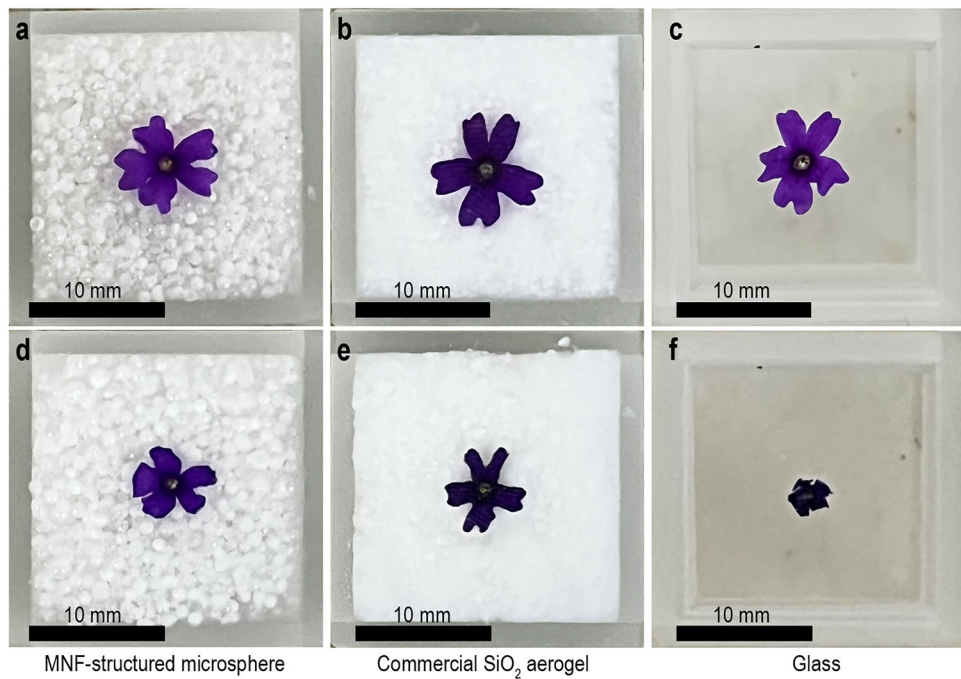


Fig. 5 | Proof-of-concept for thermal insulation performance for protecting fresh petals from withering. **a** MNF-structured microsphere compared to commercial SiO_2 aerogel (**b**) and glass (**c**) before heating. **d** MNF-structured microsphere compared to commercial SiO_2 aerogel (**e**) and glass (**f**) after heating.

microspheres and commercial SiO_2 aerogel powder were packed into $20 \times 20 \times 20 \text{ mm}^3$ glass boxes (Supplementary Fig. 23) and placed on a heating stage at 280°C (Fig. 5a, b). A blank glass plate was put on glass box as a control (Fig. 5c). Fresh petals were placed on the a-side of each box (Supplementary Fig. 23) and heated for 10 min. The petals placed on the MNF-structured microspheres (Fig. 5d) and commercial SiO_2 aerogel powder (Fig. 5e) showed only slight wilting, while those on the blank glass (Fig. 5f) were completely dried. These results indicated that the thermal insulation performance of MNF-structured microspheres was comparable to that of commercial SiO_2 aerogels and significantly superior to pure glass.

As shown in Fig. 6a, a $20 \times 20 \times 20 \text{ mm}^3$ glass box was filled with MNF-structured microspheres to test the insulation performance. When the glass box was placed on a heating stage at 100°C , a distinct temperature gradient distribution was observed by an infrared camera. After 1 min heating, the top surface temperature was about 34°C (Fig. 6b), increasing slightly to $\approx 40^\circ\text{C}$ after 30 min. The surface temperature variation was basically consistent with that of commercial SiO_2 aerogel powder when the heating condition was held constant (Fig. 6c, d).

Further, the heating stage temperature was set at 280°C . After 1 min, the top surface temperature of the MNF-structured microspheres reached $\approx 104^\circ\text{C}$, increasing slightly to $\approx 118^\circ\text{C}$ after 30 min (Fig. 6e, f). Under the same conditions, the top surface temperature of commercial SiO_2 aerogel powder reached $\approx 116^\circ\text{C}$ after 30 min (Fig. 6g, h), closely matching the performance of the MNF-structured microspheres. These results indicated that the MNF-structured microspheres provided effective thermal insulation, highlighting their potential for applications, such as double-layer insulation glass fillers, insulation coatings, etc.

Optical properties

The MNF-structured microsphere, characterized by low density, high transparency, and thermal stability, could be further functionalized for diverse applications, e.g., anti-counterfeiting. The SrAl_2O_4 particles were adopted as fluorescent additives (Supplementary Fig. 24) to change the optical properties of the MNF-structured microspheres by

DMFFS technology. Both SrAl_2O_4 and H_2SiO_3 particles were placed in induction furnace and treated for 30 s at 20 A (AC) (Fig. 7a). In the process, H_2SiO_3 particles formed MNF-structured microspheres by the DMFFS technology. The modified microspheres emitted intense blue-purple under UV light (Fig. 7b) and was denoted as fluorescent MNF-structured microsphere. The XPS analysis illustrated that the SrAl_2O_4 particles were simultaneously transported to the MNF-structured microspheres (Supplementary Fig. 25 and Fig. 7c) and the electron paramagnetic resonance (EPR) test revealed oxygen vacancy defects induced by SrAl_2O_4 doping (Fig. 7d). Photoluminescence (PL) under 320 nm laser excitation (Fig. 7e) exhibited three emission peaks centering at 385 nm, 423 nm, and 574 nm, attributed to the defect luminescence. The morphology of the fluorescent MNF-structured microspheres was consistent with that of the MNF-structured microspheres (Fig. 7f), suggesting the fluorescent substances were incorporated uniformly. Meanwhile, the EDS results indicated the uniform distribution of SrAl_2O_4 particles throughout both the inner MNF structure and shells (Fig. 7g, h). These results demonstrated that DMFFS enabled effective transport of the fluorescent additives into MNF-structured microspheres, imparting tunable optical properties.

Despite fluorescent MNF-structured microspheres were difficult to identify under sunlight due to their transparent appearance (Fig. 7i), the fluorescent microspheres emitted a distinct blue-purple glow under UV irradiation (Fig. 7j), highlighting their potential in anti-counterfeiting applications.

Moreover, after soaking the MNF-structured microspheres for 12 h in solution of yellow-green-emitting SrAl_2O_4 , blue-emitting $\text{CaSrAlO: Eu}^{2+}, \text{Dy}^{3+}$, and red-emitting Eu_2O_3 , the MNF-structured microspheres would absorb these powders and emit yellow-green light (Fig. 8a), blue light (Fig. 8d), and red light (Fig. 8g) under UV light, respectively. When the MNF-structured microspheres after soaking mixed with commercial SiO_2 aerogel powder, the mixtures were indistinguishable under daylight (Fig. 8b, e, h), but revealed strong yellow-green (Fig. 8c), blue (Fig. 8f), and red (Fig. 8i) emission under UV light. These results demonstrated the potential of MNF-structured microspheres as anti-counterfeiting agents for aerogel-based materials. The advantages of this system towards application included: (i)

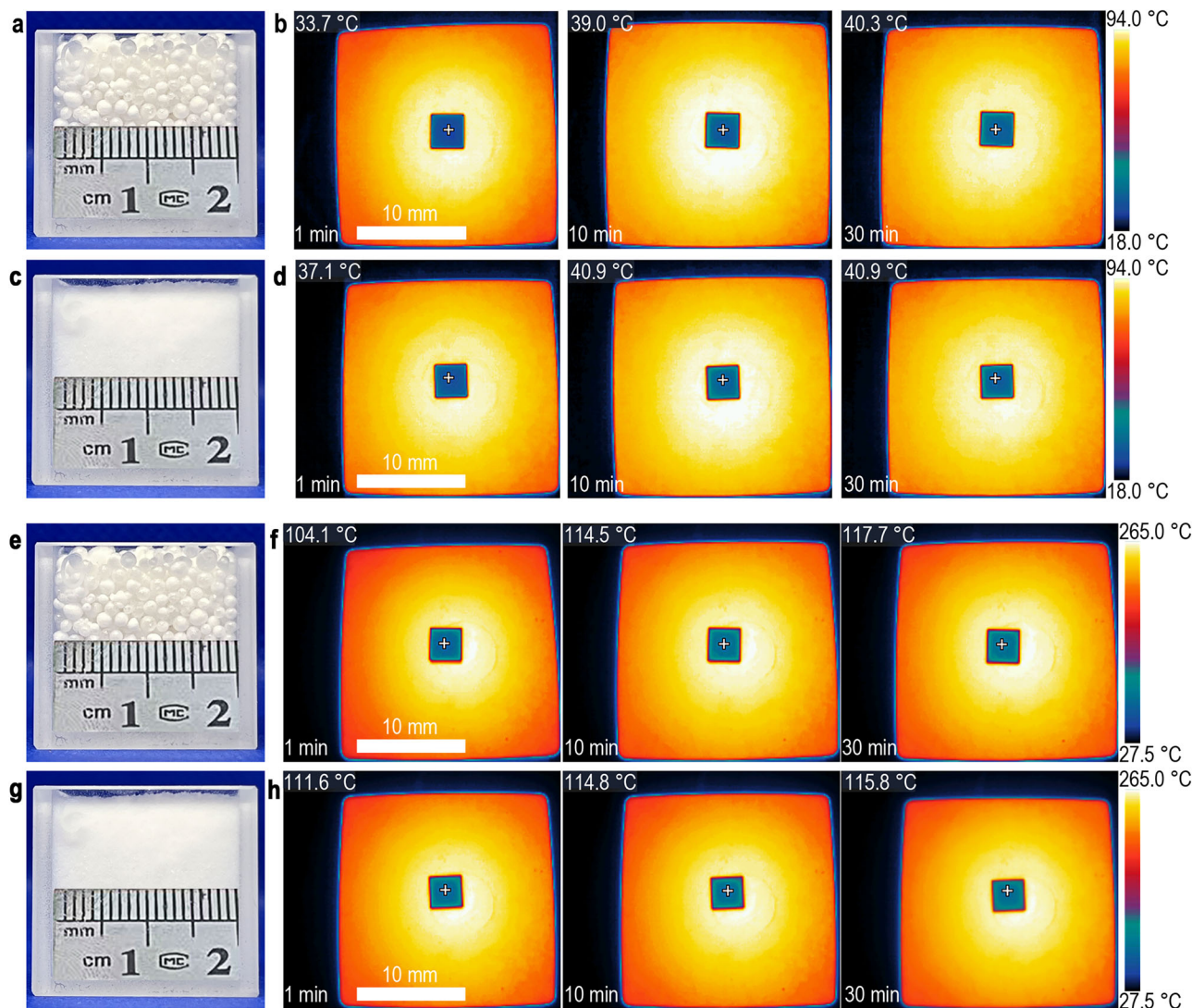


Fig. 6 | Thermal insulation properties of the MNF-structured microsphere compared with commercial SiO_2 aerogel powder. **a, b** Optical and infrared images of MNF-structured microsphere in a $20 \times 20 \times 20 \text{ mm}^3$ glass box on a heating stage at 100°C for 30 min. **c, d** Optical and infrared images of commercial

SiO_2 aerogel powder under the same conditions. **e, f** Optical and infrared images of MNF-structured microsphere in a glass box on a heating stage at 280°C for 30 min. **g, h** Optical and infrared images of commercial SiO_2 aerogel powder under the same conditions.

Self-protection, as the outer shell prevented contamination of the internal fluorescent material. (ii) Long-term stability, due to thermal stability and chemical stability. (iii) Luminous uniqueness, as the characteristic microsphere morphology was difficult to replicate. Overall, these features highlighted the potential of MNF-structured microsphere to enhance security in the aerogel market and combated counterfeit and substandard products.

Discussion

If DMFFS was applied, its magnetic field could drive the non-magnetic SiO_2 particles pivoting. According to the Barnett effect, the spinner would be magnetized along spinning axis. Under these conditions, molten SiO_2 particles were transformed into well-sealed microspheres containing abundant MNF structure. The MNF-structured microsphere exhibited low density (0.1 g cm^{-3}), high transparency ($\approx 85.6\%$), and superior thermal stability ($\approx 1200^\circ\text{C}$ in both air and argon atmosphere), yielding superior thermal insulation performance. Furthermore, fluorescent additives were transported into the microsphere during the DMFFS process, producing materials with strong UV-excited luminescence and potential applications in anti-counterfeiting.

Moreover, a sealed SiO_2 hollow microsphere with NF structure interior could be obtained by extending the stirring time or increasing the magnetic field strength. In conclusion, the DMFFS technique provided a rapid and scalable strategy for the mass production of SiO_2 microspheres containing SiO_2 micro/nano-sized fibers, while also established a path for manipulating non-magnetic materials via magnetic fields.

Methods

Materials

H_2SiO_3 particles (Macklin, 99.7%, S902507), SrAl_2O_4 (Rhawn, 800 mesh, R138129), Eu_2O_3 (Damas-beta, 99.99%, 19791 A), $\text{CaSrAlO} : \text{Eu}^{2+}, \text{Dy}^{3+}$ (Usolf, 250 mesh, MHSB-9C).

Syntheses

Preparation of the SiO_2 -15 particles: Firstly, 0.25 g H_2SiO_3 was put into a 2 mL graphite crucible in vacuum environment. Secondly, the graphite crucible was placed into the induction coil and turned on the induction heating machine at 20 A (AC). Lastly, the reaction continued for 15 s to obtain SiO_2 -15 particle.

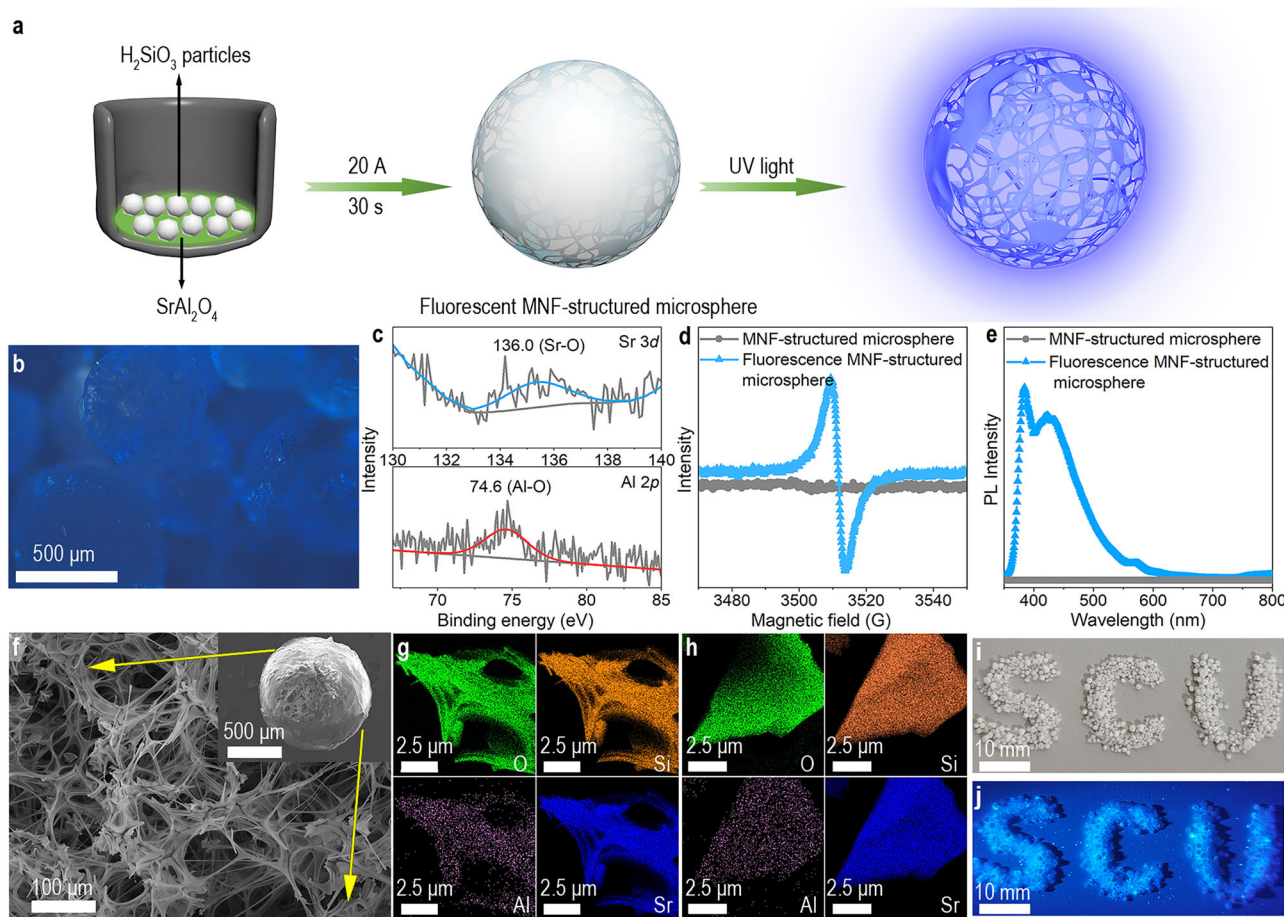


Fig. 7 | Optical properties of fluorescent MNF-structured microsphere. **a** The diagram of synthesis mechanism of fluorescent MNF-structured microsphere. **b** The optical image of fluorescent MNF-structured microsphere under UV light by the fluorescence microscope, showing intense blue-purple. The experiment was independently repeated a minimum of three times. **c** High resolution Al 2p and Sr 3d XPS spectra. **d** The EPR spectra of MNF-structured microsphere and fluorescence MNF-structured microsphere (the gray represented MNF-structured microsphere, the blue represented fluorescent MNF-structured microsphere). **e** The PL spectra with 320 nm excitations of MNF-structured microsphere and fluorescence

MNF-structured microsphere (the gray represented MNF-structured microsphere, the blue represented fluorescent MNF-structured microsphere). **f** The internal SEM image of inside fluorescent MNF-structured microsphere. The insert SEM image of **(f)** was the whole fluorescent MNF-structured microsphere. The experiment was independently repeated a minimum of three times. **g** The EDS image of skeletons, **(h)** the EDS image of shells. **i** The photograph of the fluorescent MNF-structured microsphere under sunlight. **j** The photograph of the fluorescent MNF-structured microsphere under UV light. Source data are provided as a Source Data file.

Preparation of the MC20 microsphere: Firstly, 0.25 g H_2SiO_3 was put into a 2 mL graphite crucible in vacuum environment. Secondly, the graphite crucible was placed into the induction coil and turned on the induction heating machine at 20 A (AC). Lastly, the reaction continued for 20 s to obtain MC20 microsphere.

Preparation of the MNF-structured microsphere: Firstly, 0.25 g H_2SiO_3 was put into the 2 mL graphite crucible in a vacuum environment. Secondly, the graphite crucible was placed into the induction coil and turned on the induction heating machine at 20 A (AC). Lastly, the reaction continued for 30 s to obtain the MNF-structured microsphere.

Preparation of the NF-structured microsphere: Firstly, 0.1 g MC20 microsphere were put into the 2 mL graphite crucible in vacuum environment. Secondly, the graphite crucible was placed into the induction coil and turned on the induction heating machine at 20 A (AC). Lastly, the reaction continued for 30 s to obtain the NF-structured microsphere.

Preparation of the NF-structured microsphere: Firstly, 0.25 g H_2SiO_3 was put into the 2 mL graphite crucible in vacuum environment. Secondly, the graphite crucible was placed into the induction coil and turned on the induction heating machine at 22 A. Lastly, the reaction continued for 25 s to obtain the NF-structured microsphere.

Preparation of the SiO_2 -1100 °C particles: 1 g H_2SiO_3 was put into tube furnace and annealed at 1100 °C for 1 min under vacuum environment with a heating rate of 8 °C min^{-1} to obtain SiO_2 -1100 °C particles.

Preparation of the fluorescent MNF-structured microsphere: Firstly, 0.02 g SrAl_2O_4 was put into a 2 mL graphite crucible and covered with 0.20 g H_2SiO_3 in vacuum environment. Secondly, the graphite crucible was placed into the induction coil and turned on the induction heating machine at 20 A (AC). Lastly, the reaction continued for 30 s to obtain the fluorescent MNF-structured microsphere.

Method of deducting diamagnetic background

For the linear part under high field strength, we used the formula: $y = y_0 - kx$ to deduct the linear background, where x referred to the field strength in the original data, y referred to the magnetization, and k was the slope of the linear part.

Characterization

The morphologies of all samples were observed using field emission scanning electron microscope (FE-SEM, JSM-7610F, 5 kV or 10 kV). The transmission electron microscopy (TEM), high-resolution transmission electron microscopy (HRTEM), and energy-dispersive X-ray

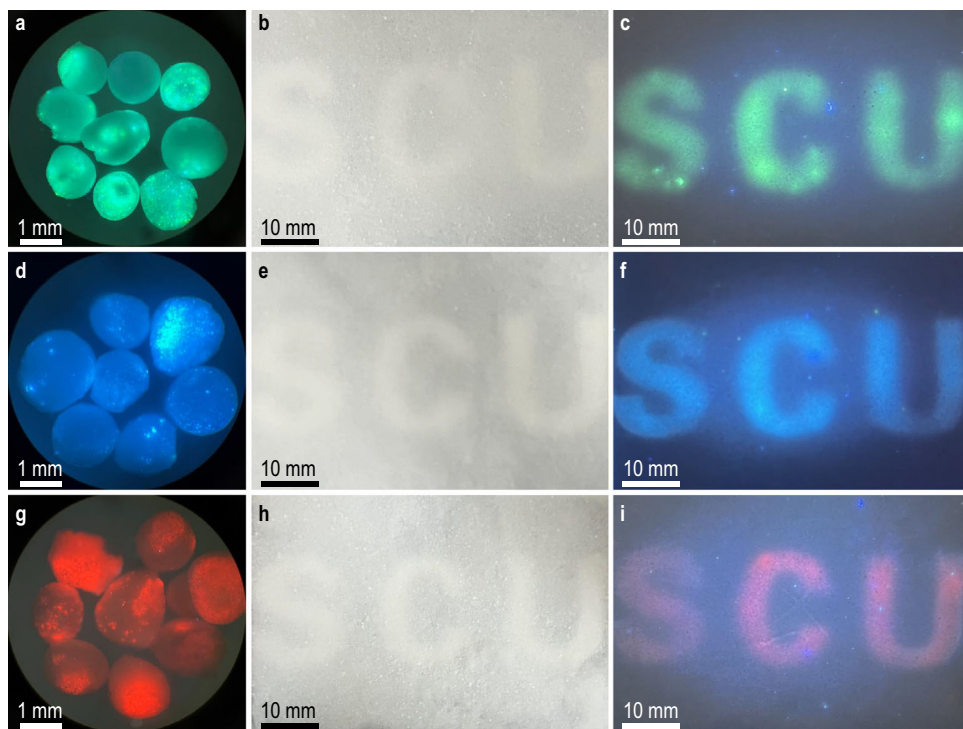


Fig. 8 | The anti-counterfeiting application of MNF-structured microsphere in SiO_2 aerogel. **a** Microphotograph of MNF-structured microsphere after being soaked in a yellow-green-emitting SrAl_2O_4 solution for 12 h under UV light. **b** Photograph of the mixture under sunlight. **c** Photograph of the mixture under UV light. **d** Microphotograph of MNF-structured microsphere after being soaked in a blue-emitting $\text{CaSrAlO}_3\text{:Eu}^{2+}, \text{Dy}^{3+}$ solution for 12 h under UV light. **e** Photograph of the mixture under sunlight. **f** Photograph of the mixture under UV light. **g** Microphotograph of MNF-structured microsphere after being soaked in a red-emitting Eu_2O_3 solution for 12 h under UV light. **h** Photograph of the mixture under sunlight. **i** Photograph of the mixture under UV light. All experiments were independently repeated a minimum of three times.

the mixture under sunlight. **f** Photograph of the mixture under UV light. **g** Microphotograph of MNF-structured microsphere after being soaked in a red-emitting Eu_2O_3 solution for 12 h under UV light. **h** Photograph of the mixture under sunlight. **i** Photograph of the mixture under UV light. All experiments were independently repeated a minimum of three times.

spectroscopy mapping (EDS) were obtained by JEM-F200, 200 kV. The X-ray photoelectron spectroscopy (XPS) of all samples was collected by Thermo Scientific K-Alpha (Al K_α , 12 kV, 6 mA). X-ray diffraction (XRD) patterns were collected by EMPYREAN (Cu K_α , 40 kV, 40 mA). Raman spectra of all samples were tested using a Raman spectrometer (Thermo Scientific DXR) with a 532 nm laser light at room temperature. The total transmission spectra were recorded using the ultraviolet through visible and near-infrared spectra (UV2100). Thermo-gravimetry analyses (TGA) were tested (TGA-DSC, Mettler Toledo TGA/DSC 3+, Switzerland) in both air and argon atmosphere with heating from room temperature to 1200 °C at a rate of 10 °C min⁻¹. TGA, DSC and mass spectrometry data were simultaneously characterized by a STA 449F3 Jupiter® simultaneous thermal analyzer (Erich NETZSCH GmbH & Co. Holding KG. The DSC data in the TGA-DSC combined equipment is for reference only), which was combined with a QMS 403D Aeolos Quadropole mass spectrometer (Erich NETZSCH GmbH & Co. Holding KG). The FT-IR spectra were collected by infrared spectrometer (NEXUS 670). The optical images were collected with a fluorescence microscope (HS600E). The infrared images were collected by an infrared thermal camera (HIMICRO, H10S+). The photoluminescence (PL) quenching data were measured by a steady-state and transient fluorescence spectrometer (Fluorolog-3). Electron paramagnetic resonance (EPR) was tested by Bruker EMXplus.

Reporting summary

Further information on research design is available in the Nature Portfolio Reporting Summary linked to this article.

Data availability

The data supporting the findings of this study are available from the corresponding author upon request. Unprocessed data, including

uncropped images, are provided as Supplementary Data 1. Source data are provided with this paper.

References

1. Wang, Y. et al. Bioinspired enzymatic compartments constructed by spatiotemporally confined *in situ* self-assembly of catalytic peptide. *Commun. Chem.* **5**, 81 (2022).
2. Li, H. H. & Yu, S. H. Recent advances on controlled synthesis and engineering of hollow alloyed nanotubes for electrocatalysis. *Adv. Mater.* **31**, 1803503 (2019).
3. Huang, K. et al. Hollow-structured metal oxides as oxygen-related catalysts. *Adv. Mater.* **31**, 1801430 (2018).
4. Wang, Y., Yu, L. & Lou, X. W. Formation of triple-shelled molybdenum-polydopamine hollow spheres and their conversion into MoO_2 /Carbon composite hollow spheres for lithium-ion batteries. *Angew. Chem. Int. Ed.* **55**, 14668–14672 (2016).
5. Wang, Z. & Zhou, L. X. W. David Lou, Metal oxide hollow nanostructures for lithium-ion batteries. *Adv. Mater.* **24**, 1903–1911 (2012).
6. Sim, S., Oh, P., Park, S. & Cho, J. Critical thickness of SiO_2 coating layer on core@shell bulk@nanowire Si anode materials for Li-ion batteries. *Adv. Mater.* **25**, 4498–4503 (2013).
7. Kumar, S., Srivastava, R., Pak, D. & Chattopadhyay, J. Synthesis and energy applications of multi-shell micro/nano-spheres. *Int. J. Energ. Res.* **45**, 14389–14413 (2021).
8. Roberts, S. et al. Complex microparticle architectures from stimuli-responsive intrinsically disordered protein. *Nat. commun.* **11**, 1342 (2020).
9. Zhao, D., Wei, Y., Xiong, J., Gao, C. & Wang, D. Response and regulation of the microenvironment based on hollow structured drug delivery systems. *Adv. Funct. Mater.* **33**, 2300681 (2023).

10. Zhao, D. et al. Sequential drug release via chemical diffusion and physical barriers enabled by hollow multishelled structures. *Nat. commun.* **11**, 4450 (2020).
11. Zhou, L. et al. Intricate hollow structures: controlled synthesis and applications in energy storage and conversion. *Adv. Mater.* **29**, 1602914 (2017).
12. Yu, L., Hu, H., Wu, H. B. & Lou, X. W. Complex hollow nanostructures: synthesis and energy-related applications. *Adv. Mater.* **29**, 1604563 (2017).
13. Wang, J., Wan, J. & Wang, D. Hollow multishelled structures for promising applications: understanding the structure–performance correlation. *Acc. Chem. Res.* **52**, 2169–2178 (2019).
14. Li, Z., Li, B., Yu, C., Wang, H. & Li, Q. Recent progress of hollow carbon nanocages: general design fundamentals and diversified electrochemical applications. *Adv. Sci.* **10**, 2206605 (2023).
15. Iskandar, F. et al. Controllability of pore size and porosity on self-organized porous silica particles. *Nano. Lett.* **2**, 389–392 (2002).
16. Ma, Y. et al. Remodeling nanodroplets into hierarchical mesoporous silica nanoreactors with multiple chambers. *Nat. commun.* **13**, 6136 (2022).
17. Zhang, W. M. et al. Tin-nanoparticles encapsulated in elastic hollow carbon spheres for high-performance anode material in lithium-ion batteries. *Adv. Mater.* **20**, 1160–1165 (2008).
18. Liao, J. et al. 3D core-shell $\text{Fe}_3\text{O}_4@\text{SiO}_2@\text{MoS}_2$ composites with enhanced microwave absorption performance. *J. Colloid Interf. Sci.* **604**, 537–549 (2021).
19. Yu, Y., Wang, Q., Dai, J., Li, Y. & Wang, C. One-step morphology control synthesis of coaxial $\text{MgCo}_2\text{O}_4@\text{Mn}_2\text{O}_3$ hollow core-shell structures by electrospinning. *Micropor. Mesopor. Mat.* **351**, 112489 (2023).
20. Wei, Y. et al. Coaxial 3D printing of zeolite-based core–shell monolithic Cu-SSZ-13@ SiO_2 catalysts for diesel exhaust treatment. *Adv. Mater.* **36**, 2302912. (2023).
21. Chen, H., Zhao, Y., Song, Y. & Jiang, L. One-step multicomponent encapsulation by compound-fluidic electrospray. *J. Am. Chem. Soc.* **130**, 7800–7801 (2008).
22. Wang, T. et al. Competition among refined hollow structures in Schiff base polymer derived carbon microspheres. *Nano. Lett.* **22**, 3691–3698 (2022).
23. Wang, T. et al. Space-confined polymerization: controlled fabrication of nitrogen-doped polymer and carbon microspheres with refined hierarchical architectures. *Adv. Mater.* **31**, 1807876 (2019).
24. Wei, Y., Wang, J., Yu, R., Wan, J. & Wang, D. Constructing $\text{SrTiO}_3\text{-TiO}_2$ heterogeneous hollow multi-shelled structures for enhanced solar water splitting. *Angew. Chem. Int. Ed.* **58**, 1422–1426 (2019).
25. Teng, Z. et al. A facile multi-interface transformation approach to monodisperse multiple-shelled periodic mesoporous organosilica hollow spheres. *J. Am. Chem. Soc.* **137**, 7935–7944 (2015).
26. Liu, X.-F., Lai, Y.-K., Huang, J.-Y., Al-Deyab, S. S. & Zhang, K.-Q. Hierarchical $\text{SiO}_2@\text{Bi}_2\text{O}_3$ core/shell electrospun fibers for infrared stealth camouflage. *J. Mater. Chem. C.* **3**, 345–351 (2015).
27. Ma, Y. & Qi, L. Solution-phase synthesis of inorganic hollow structures by templating strategies. *J. Colloid Interf. Sci.* **335**, 1–10 (2009).
28. Wang, J. et al. Accurate control of multishelled Co_3O_4 hollow microspheres as high-performance anode materials in lithium-ion batteries. *Angew. Chem. Int. Ed.* **52**, 6417–6420 (2013).
29. Zhou, Q. et al. Template-guided synthesis of Co nanoparticles embedded in hollow nitrogen doped carbon tubes as a highly efficient catalyst for rechargeable Zn-air batteries. *Nano Energy* **71**, 104592 (2020).
30. Qi, J. et al. Multi-shelled hollow micro-/nanostructures. *Chem. Soc. Rev.* **44**, 6749–6773 (2015).
31. Zhao, H. et al. Hierarchical assembly of multilayered hollow microspheres from an amphiphilic pharmaceutical molecule of azithromycin. *Adv. Mater.* **20**, 3682–3686 (2008).
32. Dong, Z. et al. 3D printing of inherently nanoporous polymers via polymerization-induced phase separation. *Nat. Commun.* **12**, 247 (2021).
33. Liang, Y., Zhu, Z., Li, Q. & Huang, Q. Developing a dynamic magnetic flux template to guide 1D nanomaterial growth. *Chem. Commun.* **58**, 10245–10248 (2022).
34. Zhou, W. T., Liu, Q. & Huang, Q. S. Reversing silicon carbide into 1D silicon nanowires and graphene-like structures using a dynamic magnetic flux template. *Mater. Horiz.* **10**, 1354–1362 (2023).
35. Qiao, X., Qi, R., Gao, F. & Huang, Q. Capture of $\text{SiC}/\text{amorphous SiO}_2$ core–shell nanowires from rice husk ash within 25 seconds by dynamic magnetic field. *Ceram. Int.* **51**, 54013–54020 (2025).
36. Xia, C. et al. Synthesis of $\text{Al}_2\text{O}_3\text{-SiO}_2$ aerogel from water glass with high thermal stability and low thermal conductivity. *J. Sol.-Gel. Sci. Techn.* **106**, 561–571 (2023).
37. Nie, F., Wang, K. Z. & Yan, D. Supramolecular glasses with color-tunable circularly polarized afterglow through evaporation-induced self-assembly of chiral metal-organic complexes. *Nat. Commun.* **14**, 1654 (2023).
38. Ma, J., Song, C., Chen, S., Xu, Y. & Du, H. Drop-casting preparation of a binder-free SiO_x anode with micron-sized SiO_x particles for high-performance lithium-ion batteries. *J. Alloy. Compd.* **918**, 165682 (2022).
39. Liu, T. et al. Core-shell structured $\text{C}@\text{SiO}_2$ hollow spheres decorated with Nickel nanoparticles as anode materials for lithium-ion batteries. *Small* **17**, e2103673 (2021).
40. He, S. et al. Effect of heat treatment on hydrophobic silica aerogel. *J. Hazard. Mater.* **362**, 294–302 (2019).
41. Zeng, Q., Li, K., Fen-chong, T. & Dangla, P. Pore structure characterization of cement pastes blended with high-volume fly-ash. *Cem. Concr. Res.* **42**, 194–204 (2012).

Acknowledgements

This work was supported partly by grants from the National Natural Science Foundation of China (No. 51771125) and the Tianfu Jiangxi Laboratory FY2024 Achievement Transformation Grant Funding Program. We thank Ms Yanping Huang from the Engineering Experimental Teaching Center, School of Chemical Engineering (SEM and TEM). We would like to thank Dr. Wu Peng and Dr. Yanying Wang of Analytical & Testing Center Sichuan University for their assistance on steady/transient fluorescence. We thank Ms Shaolan Wang from the Analytical & Testing Center Sichuan University for her assistance on TGA/DSC test. We thank Dr. Feng Yang from the Comprehensive Training Platform of the Specialized Laboratory in the College of Chemistry at Sichuan University for her assistance on TEM test. We thank Ms Yue Qi for the XRD measurements at the comprehensive training platform of the Specialized Laboratory in the College of Chemistry, Sichuan University.

Author contributions

X.H.Q. and Q.S.H. conceived and designed the research. X.H.Q. led the materials preparation and tests. J.Q.L. participated in the SEM characterization. X.H.Q., Q.S.H., and R.F.Q. discussed the results and analyzed the data. X.H.Q. wrote the paper. Q.S.H. supervised the research.

Competing interests

The authors declare no competing interests.

Additional information

Supplementary information The online version contains supplementary material available at <https://doi.org/10.1038/s41467-025-67205-6>.

Correspondence and requests for materials should be addressed to Qingsong Huang.

Peer review information *Nature Communications* thanks Zhen-An Qiao, and the other, anonymous, reviewers for their contribution to the peer review of this work. A peer review file is available.

Reprints and permissions information is available at <http://www.nature.com/reprints>

Publisher's note Springer Nature remains neutral with regard to jurisdictional claims in published maps and institutional affiliations.

Open Access This article is licensed under a Creative Commons Attribution-NonCommercial-NoDerivatives 4.0 International License, which permits any non-commercial use, sharing, distribution and reproduction in any medium or format, as long as you give appropriate credit to the original author(s) and the source, provide a link to the Creative Commons licence, and indicate if you modified the licensed material. You do not have permission under this licence to share adapted material derived from this article or parts of it. The images or other third party material in this article are included in the article's Creative Commons licence, unless indicated otherwise in a credit line to the material. If material is not included in the article's Creative Commons licence and your intended use is not permitted by statutory regulation or exceeds the permitted use, you will need to obtain permission directly from the copyright holder. To view a copy of this licence, visit <http://creativecommons.org/licenses/by-nc-nd/4.0/>.

© The Author(s) 2025